

A quantitative analysis of the cone-angle dependence in precession electron diffraction

J. Ciston^{a,*}, B. Deng^a, L.D. Marks^a, C.S. Own^a, W. Sinkler^b

^a*Department of Materials Science and Engineering, Northwestern University, Evanston, IL 60208, USA*

^b*UOP LLC, Des Plaines, IL 60017, USA*

Received 16 February 2007; received in revised form 29 June 2007; accepted 1 August 2007

Abstract

Precession electron diffraction (PED) is a technique which is gaining increasing interest due to its ease of use and reduction of the dynamical scattering problem in electron diffraction. To further investigate the usefulness of this technique, we have performed a systematic study of the effect of precession angle on the mineral andalusite where the semiangle was varied from 6.5 to 32 mrad in five discrete steps. The purpose of this study was to determine the optimal conditions for the amelioration of kinematically forbidden reflections, and the measurement of valence charge density. We show that the intensities of kinematically forbidden reflections decay exponentially as the precession semiangle (φ) is increased. We have also determined that charge density effects are best observed at moderately low angles (6.5–13 mrad) even though PED patterns become more kinematical in nature as the precession angle is increased further.

© 2007 Elsevier B.V. All rights reserved.

PACS: 61.14.–x; 71.20–b; 61.50.Ah

Keywords: Precession electron diffraction; Bulk charge density; Kinematical extinction; Multislice simulation

1. Introduction

The last century has witnessed great strides in our ability to measure and understand the structures of materials with a high degree of accuracy, particularly with regard to the average crystallographic structure of macroscopic materials as well as nanoscale defect phenomena. The majority of these crystallographic studies have been focused on the understanding of the atomic structure and deviations of atomic positions in an effort to correlate this information with material behavior. It is increasingly clear, however, that the behavior and structure of the valence electrons in the ground state is at least as important (though less studied) as information about the atomic cores themselves because it aides our understanding of chemical bonds and other technologically important phenomena such as doping.

It has long been known that very accurate X-ray diffraction measurements are sensitive to the subtle effects of valence charge density [1], indeed the measured structure factors are the moduli for the Fourier transform of the total charge density of a crystal after correction for known experimental phenomena. The availability of synchrotron radiation has led to a large number of experimental refinements of charge density in bulk crystals (see [2,3] for reviews) and has also been recently accomplished for a surface [4]. A caveat is that due to the small scattering cross-section that atoms present to X-rays, relatively large single crystals must be produced to increase the interaction volume and obtain suitably small intensity errors.

Electron diffraction is somewhat better suited to the measurement of charge density because the scattering cross-section of high energy electrons (100–400 keV) is approximately 10^4 larger than that of X-rays, enabling good signal-to-noise intensity measurements of nanoscale particles in a TEM. In particular, quantitative convergent beam electron diffraction (QCBED) has been extensively

*Corresponding author. Tel.: +1 847 491 7809; fax: +1 847 491 7820.
E-mail address: j-ciston@northwestern.edu (J. Ciston).

used for such measurements [5–16]. While QCBED is an excellent tool for precisely measuring charge density effects at low scattering angles, the technique cannot efficiently capture a large number of high angle reflections necessary for structural refinement. Therefore, a second technique (such as X-ray diffraction or DFT simulation) must be used to determine the atomic structure before the charge density can be experimentally refined.

Traditional selected-area or conventional parallel nano-beam electron diffraction is, in general, unsuitable for *a-priori* bulk structure determination or charge density refinement because the magnitude of dynamical effects may not be precisely measured as in the case of QCBED. One consequence of this is the appearance of reflections, which are kinematically forbidden due to the symmetry of the crystal, but are allowed via multiple scattering pathways in electron diffraction. Therefore, if the crystal structure is unknown, the observed symmetry may be misleading, or in the worst case completely incorrect.

Precession electron diffraction (PED), originally developed by Vincent and Midgley [17], is a promising technique in electron crystallography that is rapidly becoming mainstream due to the technique's reduction of the dynamical diffraction problem and improvement of transmission electron diffraction measurements. PED datasets have been shown to be "more kinematical" [17–20] due to the avoidance of the strongly excited zone-axis condition and the limitation of two-dimensional (2-D) multiple scattering pathways. One consequence of this is that in many cases kinematically forbidden reflections, which are often very strong in selected-area measurements, exhibit very low intensities in PED experiments, thereby enabling an easier path to symmetry determination and structure solution [21]. However, the precise degree of attenuation of these forbidden reflections has not yet been investigated. These benefits have led to the *a-priori* solution of a number of atomic structures [18,22–25] (among many other studies) and have recently been used to refine the valence charge density of silicon using both kinematical and dynamical refinements [26]. However, the experimental parameters which are optimally suited to the measurement of charge density effects have not been thoroughly explored.

In this study, we systematically investigate the effect of the magnitude of the precession semiangle (φ) on the ability to probe the structure of a crystal (both atomic and electronic) in an optimized manner. We have investigated experimentally the effect of precession tilt semiangle (φ) on the intensity of symmetry forbidden reflections in the [001] direction (e.g. the $(00L)$, $L = 2n + 1$) of the mineral andalusite (Al_2SiO_5). These experimental data are compared to multislice simulations using a variety of functional forms for the crystal potential. In addition, the experimental results were compared against combination DFT/multislice simulations incorporating the full charge density of the crystal to determine if the subtle bonding effects are observable using the PED technique and at what experimental conditions these effects are most apparent.

2. Methods and materials

2.1. Experimental

Andalusite is one of the three polymorphs of Al_2SiO_5 (the others being kyanite and sillimanite) and has an orthorhombic unit cell with $a = 7.7980$, $b = 7.9031$, and $c = 5.5566$ Å and a Pnm spacegroup (#58). The structure was first solved by Taylor [27] and later refined by Winter and Ghose [28] from which the unit cell parameters and atomic positions were taken for this study. The light elements in the structure make it a good candidate for charge density measurements as a large proportion of the total electrons participate in bonding. In a previous study, we found that the electron structure factors for this mineral are modified by as much as 5% by the valence charge density of the crystal at low scattering angles [29]. The sample was prepared of research grade andalusite from a natural mineral source in Santa Theresa, Minas Gerais, Brazil purchased from Ward's Natural Science in the form of ~ 0.5 – 5 mm particles. Smaller particles without cloudiness or large visible inclusions as seen under a $40\times$ binocular microscope were hand selected to be ground in ethyl alcohol to a fine powder, producing particles with an average size of a few hundred nanometers with some substantially smaller. The particle suspension was allowed to rest for 15 min to allow larger particles to settle out before the upper portion of the remaining liquid was dispersed in solution on a copper TEM grid coated with lacey carbon film.

Experimental precession data for the andalusite [110] zone axis were collected on a JEOL 3000F microscope at 300 kV in nanobeam diffraction mode modified and retrofitted with a second-generation precession system developed at Northwestern University [30]. Diffraction data sets were collected on a Gatan US1000 camera with 2×2 binning to produce 1024×1024 pixel images at 16 bits of dynamic range. Imaging conditions other than the precession angle were kept constant for all data collected. The precession system is aligned separately from the column itself and comprises an alignment of two-fold astigmatism amplitude for both the upper and lower coils as well as a relative phase adjustment for the descanned coil. Because andalusite is a somewhat beam-sensitive material, rough alignment of the precession system was performed on a slightly thick area of the specimen adjacent to the area of interest for each of the five φ angles and the parameters recorded. The specimen was then moved back into the beam and the alignments for each φ were fine-tuned and datasets were collected. The total time the area of interest was illuminated was therefore limited to approximately 30 min. Spot intensities were measured using EDM version 2.0.1 software [31,32] with the IntegBZM flag for integration. This method first calculates a linear background away from the peak, subtracts this background estimate, and integrates the total intensity of each peak. We believe this to be superior to the XCF cross-correlation method [33] for

the case of precession because the spot size and shape is relatively non-uniform due to instrument aberrations. The symmetry was taken to be p2mm and both symmetry and Friedel averaging were used to produce the final data set.

The experimental precession angle was limited to 32 mrad because above this angle, the projector lens aberrations increase dramatically, leading to an unmanageable amount of spot splitting and spiral distortion in the pattern. This is a limitation specific to the microscope used in this study and will be overcome in a future implementation by using intermediate lens alignment coils for the descanning operation instead of the currently used projector lens coils. This is expected to push the aberration threshold to over 60 mrad.

2.2. Numerical methods

Diffraction simulations were performed using the well-established multislice method. The atomic scattering factors used were taken from the relativistic Hartree–Fock computations of Doyle and Turner (DT) [34]. To adapt the calculated structure factors to our multislice image simulation [35,36] code NUMIS, we have transformed the cell of andalusite into a new cell such that the c -axis is the incident beam direction yielding:

$$\begin{aligned} a' &= [001] = 5.5566 \text{ \AA}, & b' &= [-110] = 11.0967 \text{ \AA}, \\ c' &= [110] = 11.0967 \text{ \AA}, & \alpha &= 90.76^\circ, \beta = 90.00^\circ, \\ & & \text{and } \gamma &= 90.00^\circ. \end{aligned} \quad (1)$$

Through the above transformation, the [110] direction in the original unit cell is the [001] direction in the new unit cell. For completeness, it should be noted that the multislice algorithm has an implicit translational symmetry normal to the beam direction, which is equivalent to approximating $\alpha = 90^\circ$, a minor approximation. The unit cell was divided into eight slices of 1.399 Å thickness along the beam direction [110] with atoms summed into the appropriate slice to give the slices some of the three-dimensional (3-D) character of the transformed cell. The precession cone was broken into a set of 1000 discrete off-zone tilt angles with identical φ but different azimuth which are all simulated in the multislice code. The intensities computed for each tilt are then incoherently summed to yield a complete data set with the appropriate symmetry. The details of the computational procedure have been published elsewhere [19]. In order to minimize computational artifacts, reciprocal space was sampled out to $>7.6 \text{ \AA}^{-2}$ in order to maintain $>99.5\%$ of the total scattering intensity within the sampled region, and no empirical optical potential terms were used. The same conditions were used in simulating both precessed and conventional diffraction images.

The self-consistent-field (SCF) charge density for the andalusite was calculated by the Wien2k program [37,38]. The non-spin-polarized calculation was performed using the GGA exchange-correlation potential parameterized by

Perdew et al. [39]. For comparison, the starting unrefined charge density was also calculated from a linear superposition of atomic charge densities with the use of relativistic Dirac–Slater (DS) wavefunctions [40]. Muffin-tin radii of 1.5 atomic units (a.u.) were used for Si, Al and O atoms, 400 k points were used in the Brillouin zone, and 781 radial mesh points were used to sample the muffin-tin spheres in the radial direction. The plane-wave cut-offs of $RK_{\text{max}} = 7$ and $G_{\text{max}} = 14$ were used for expanding the charge densities and potentials. The X-ray structure factors were then obtained by Fourier transformation of the converged charge density in the muffin-tin spheres and interstitial region. The structure factors were then mapped to the transformed unit cell described earlier such that the structure factors in the new cell are:

$$\begin{aligned} F(h', k', l') &= 2F(h, k, l), \\ \text{where } h' &= l, k' = h - k, \text{ and } l' = h + k. \end{aligned} \quad (2)$$

Then the obtained structure factors were converted to electron structure factors by the Mott–Bethe formula:

$$\begin{aligned} F^e(h', k', l') &= 0.023934 \frac{(Z - F^x(h', k', l'))}{s^2} \exp(-Bs^2), \\ Z &= \sum_i Z_i \exp(i2\pi(x_i h + y_i k + z_i l)), \end{aligned} \quad (3)$$

where B is the Debye–Waller factor. All Debye–Waller factors (B) were set to a fixed isotropic value of 0.3 \AA^2 for all simulations because the beam-by-beam application of the Debye–Waller factor in the Mott–Bethe formula is not easily modified to allow for individual Debye–Waller factors for each atom. However, the errors incurred by the use of a single Debye–Waller factor are minimized for the low-angle reflections which are most sensitive to charge density variations. The transformed unit cell was divided into eight slices with a thickness of 1.3994 Å. The average projected potential for each slice was calculated by

$$V_p(h', k') = F^e(h', k', 0)/8. \quad (4)$$

It is important to note that this creates a 2-D potential projected through the full unit cell (atomic-string potential) for the DS and SCF cases due to the summation over the unit cell whereas the DT potential treats separately eight projections through 1/8 of the unit cell, thereby incorporating some information about the third-dimension. While this method of handling the potential ignores higher-order Laue zone (HOLZ) reflections, since HOLZ diffraction occurs predominantly at quite large angles we can expect the effects to be small in the low-angle bonding order regime. The SCF-derived potential was then input into the NUMIS multislice code and PED patterns were simulated in the manner described previously.

3. Results

Comparisons between experimental results and simulation were made using the conventional R factor

defined as

$$R = \frac{\sum_g |\alpha |F_g^{\text{exp}}| - |F_g^{\text{calc}}|}{\sum_g |F_g^{\text{calc}}|}, \quad (5)$$

where F_g^{exp} is the experimentally measured amplitude of the reflection located at the vector g from the origin, F_g^{calc} is the simulated amplitude, and α is the experimental scale factor. In order to properly compare experimental and simulated structure factors, α was refined to minimize the R -factor at each simulated thickness. This scaling yields very similar results to fixing α such that the (002) reflection is unity because it is the strongest non-forbidden reflection and least prone to experimental error.

3.1. Kinematical extinctions

Before discussing the specific numbers, it is relevant to clarify the type of extinction that is pertinent to our discussion. In the limit of purely kinematical diffraction, structure factors may exhibit identically zero intensity in two general cases. The first is the presence of glide planes and/or screw axes, and the second is due to increased site symmetry for atoms on special Wyckoff sites [41]. However, in highly dynamical electron diffraction experiments the issue of dynamical extinctions and bonding effects must also be addressed. There are (at least) five distinct circumstances under which kinematical extinctions may be observed in dynamical experiments which are worth note:

- Extinctions due to glide planes and/or screw axes that do not satisfy the Gjonnes–Moodie orientation conditions [42], and are generally dynamically allowed.
- Extinctions due to glide planes and/or screw axes that satisfy the Gjonnes–Moodie orientation conditions [42], and are kinematically and dynamically forbidden on the zone axis and for tilts off the zone which preserve the relevant symmetry operation.
- Accidental forbidden spots such as Si(2 2 2) which have a zero structure factor only for spherical atoms and are not forbidden when bonding effects are included, and in general are dynamically allowed. This case exists in the purely kinematical case (i.e. X-ray), but is much more apparent in electron diffraction where bonding effects are more easily observed.
- General forbidden reflections due to Wyckoff positions which have a zero structure factor even when bonding effects are included but are dynamically allowed at any orientation.
- Unconditional extinctions in which neither dynamical nor kinematical diffraction provide a scattering path, for instance (001) in an fcc material. These extinctions are the result of choosing a non-primitive Bravais lattice.

The reflections of interest here (andalusite (00 L), $L = 2n + 1$) fall into the first class.

PED datasets were collected for 6.5, 13, 18, 24, and 32 mrad φ in addition to a non-precessed pattern. R -factors were computed for DT, DS, and SCF potentials for all experimental φ angles in the range of 0–140 nm thickness. Without precession, it was very difficult to determine the thickness of the crystal via multislice simulations by locating the minimum R -factor in a zone-axis pattern. In the case of non-precessed data, there are multiple non-systematic local minima at approximately 31, 42, 14, 102, and 123 nm in order of increasing R -factor (Fig. 1(a)). This predicament is easily resolved using PED where there is a clear global minimum in the R -factor regardless of which of the three potentials is used to interpret the experimental data. The thickness at the global minimum R -factor is plotted in Fig. 1(b) for all precession angles and potentials. The SCF thickness is in all cases greater than the result from either the DT or DS neutral atom cases. This is expected due to the slightly more delocalized potential when bonding is taken into account leading to somewhat weaker scattering behavior. It is somewhat arbitrary at this stage which potential and experimental conditions are applied to determine the true thickness, so we have chosen the combination of the most kinematical precession angle (32 mrad) and the most correct potential (at least in principle), the SCF potential. From these assumptions, the thickness of the crystal was determined to be 102 nm.

The experimental and SCF-simulated datasets for all of the precession conditions at a thickness of 712 slices (100 nm) are plotted in Fig. 2 along with a circle representing the reciprocal space equivalent of the experimental precession angle. (The DT and DS fits are similar in character and are not shown here, but will be discussed later.) In the non-precessed pattern the forbidden (001) reflection has a higher experimental intensity than the allowed (002) which is consistent with multislice simulations. As the precession angle increases, two primary effects are seen: reflection intensities no longer decrease monotonically with increasing order away from the origin, and the kinematically forbidden reflections decay rapidly.

The intensities of the (001) and (003) reflections are plotted in a semi-logarithmic fashion against the precession angle yielding nearly straight lines (Fig. 3(a)) which implies an exponential decay. The allowed (002) reflection decays rather linearly and is plotted on linear axes in Fig. 3(b). To quantitatively determine the rate of decay, this intensity (I) data was fit to a simple two-parameter exponential:

$$I(\varphi) = A \exp(D\varphi), \quad (6)$$

where the amplitude (A) and decay (D) parameters were varied to produce the largest correlation coefficient (R^2). It is only the decay parameter which is of interest since the amplitude depends on the linear scaling factor applied to the intensities. The intensities for the forbidden (001) and (003) reflections were also simulated in multislice as a function of precession angle for the DT, DS, and SCF potentials. The simulated decays of the intensities were also fitted to exponentials with correlation coefficients greater

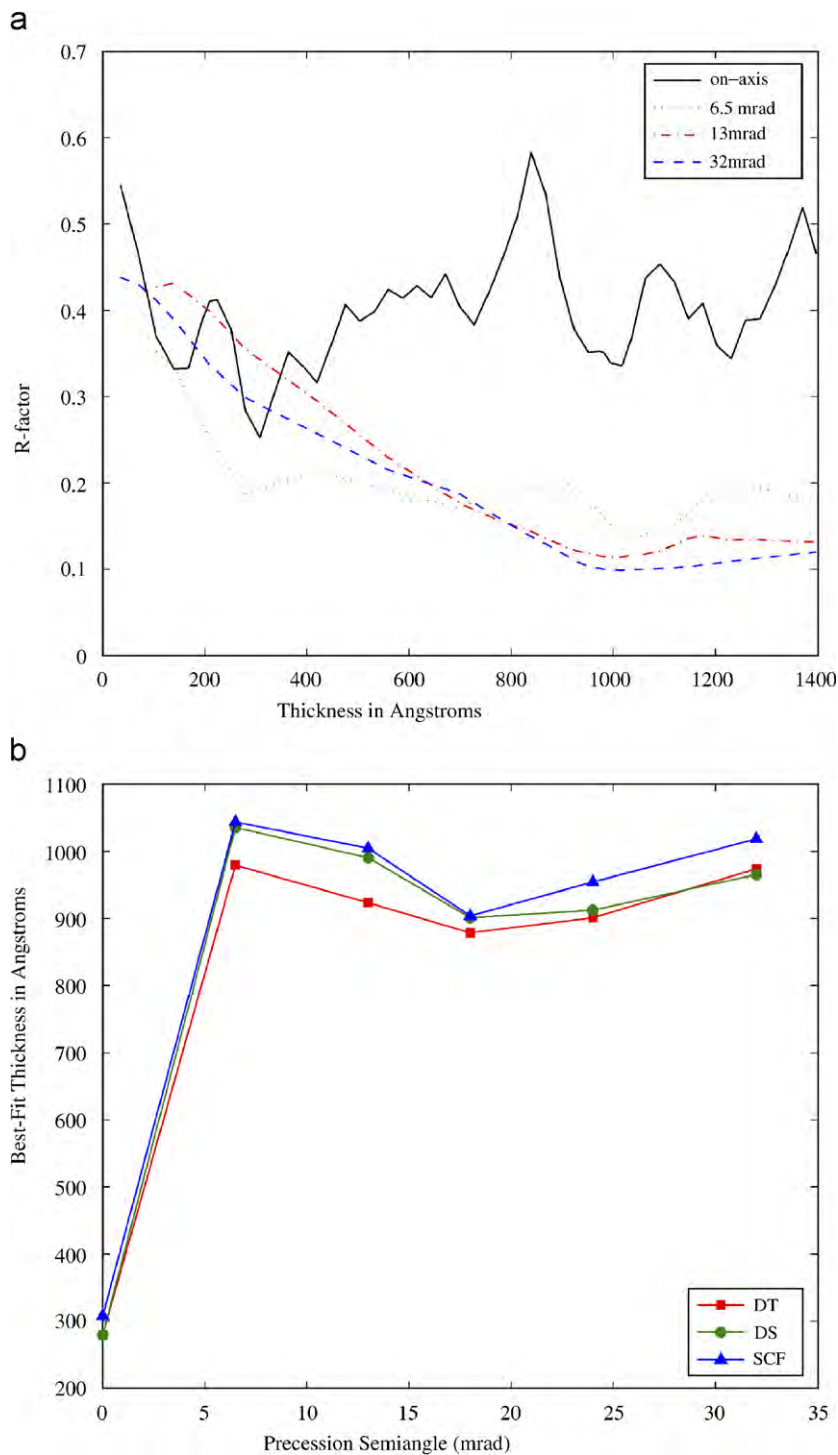


Fig. 1. (a) R -factor vs. sample thickness for precession angles of 0, 6.5, 13, and 32 mrad (18 and 24 mrad omitted for clarity) using an SCF potential and (b) best-fit thickness for all experimental precession ϕ and simulated potentials.

than 0.94 implying that the functional form of the exponential is correct for this thickness (102 nm). A summary of the fitting results is shown in Table 1. In the case for both reflections studied, the result obtained using the DT potential yielded a decay parameter most similar to the experimental result.

For the exponential form of the decay to have general validity, it must not be a fortuitous consequence of the

particular thickness observed experimentally (102 nm). Therefore, the effect of thickness was probed by fitting the DT potential simulations to the same two-parameter exponential used previously. The DT potential was chosen because it yields the closest match to the experimental decay for this case. The diffraction data are normalized to the incident beam intensity and are shown for thicknesses of 200, 300, 400, 500, 600, 728, 800, and 900 slices (28, 42,

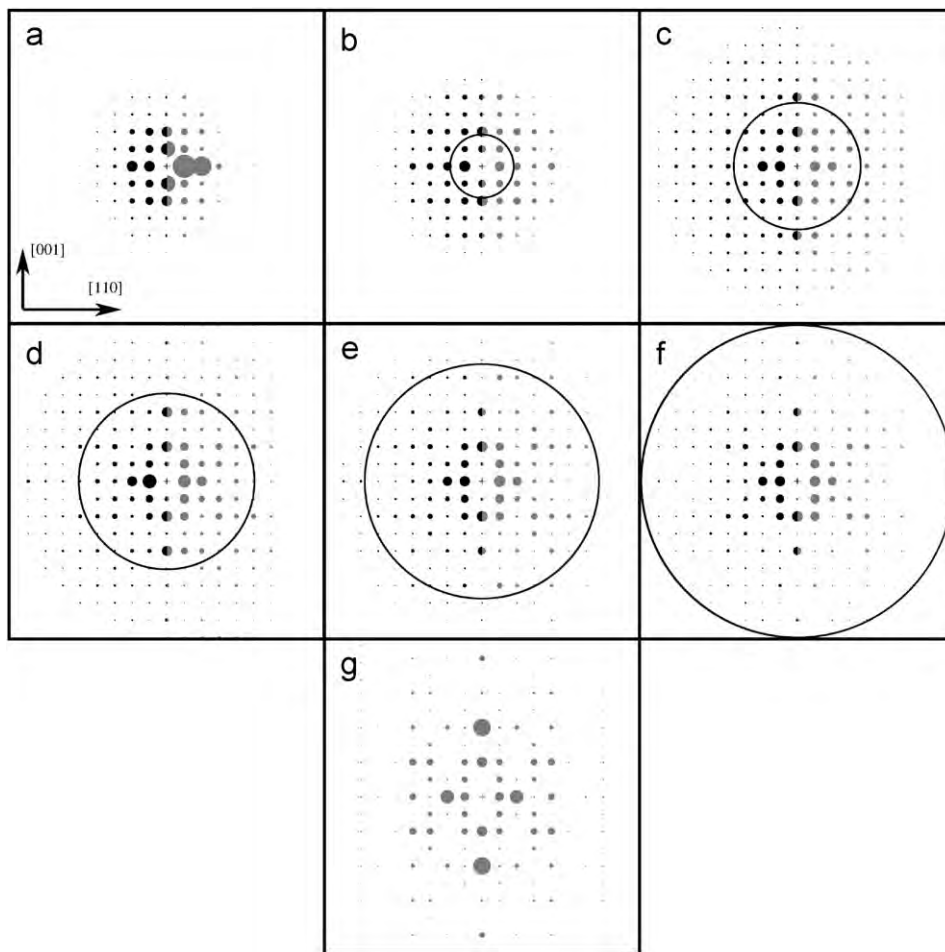


Fig. 2. Experimental (black) and simulated SCF (gray) diffraction patterns (intensity proportional to area) for the $[110]$ zone axis at 100 nm (712 slices) thickness with precession angles of (a) 0 mrad, (b) 6.5 mrad, (c) 13 mrad, (d) 18 mrad, (e) 24 mrad, (f) 32 mrad, and (g) kinematical simulation; precession circles drawn to scale (b–f). $[001]$ Direction is vertical in this figure.

56, 70, 84, 102, 112, and 126 nm) in Table 2. The functional form of the decay is indeed independent of thickness as evidenced by the large correlation coefficients. The linear amplitude constant (A) varies greatly with thickness, but is again merely an effect of scaling and is not shown. Of perhaps greatest significance is the observation that the exponential decay term is relatively invariant of thickness for each reflection: -0.112 ± 0.012 for $I(001)$ and -0.164 ± 0.015 for $I(003)$. This implies that, at least for this range of thickness, the rate at which a kinematical reflection decays with increasing precession angle is largely a fundamental property of only the crystal structure, and is less dependent on the precise amount of dynamical diffraction which increases with thickness.

3.2. Crystal misorientation

To limit the total illumination time of the specimen, the sample tilt was not fine-tuned to the zone axis as one would do in the case of QCBED because PED is forgiving of misorientation, especially with large φ . To determine the amount of zone-axis misalignment, the non-precessed

dataset was refined against both DT and SCF potentials at various off-zone misorientations. By minimizing the R -factor as a function of offset angle, it was found that the non-precessed dataset was actually collected at 0.8–0.9 mrad off-axis in the $[001]$ direction. A full set of precession calculations were performed with a 0.9 mrad offset to the precession multislice and compared with the experimental data at all PED angles.

The R -factors obtained when comparing the mistilted simulations to the unsymmetrized experimental dataset are slightly better ($<4\%$) at large precession angles than those obtained from on-axis simulations and $p2mm$ symmetrized data used to generate Fig. 1. However, for low values of φ , where the effect of charge density should be most prominent, the converse is true with the symmetrized on-axis simulations being superior, but the deviation is again small. We propose that this similarity of fit between the (incorrectly) assumed on-axis simulations and mistilted simulations as well as the low values of R -factors ($R = 0.09$ – 0.15 for the full tilt range) implies that moderate misalignment of a crystal can be safely ignored in PED experiments with the benefit of reducing the amount of

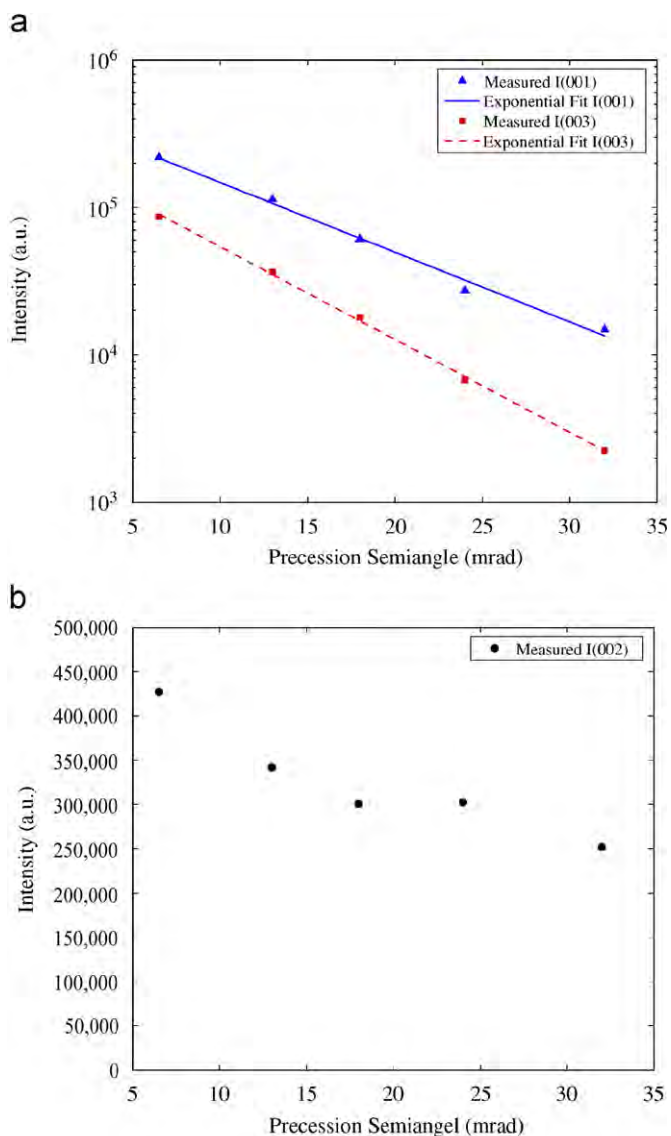


Fig. 3. (a) Plot of the intensity of the kinematically forbidden (001) and (003) reflections for each experimental φ with fitted exponentials. (b) Plot of the intensity of the measured (002) reflections as a function of semiangle.

beam damage to the crystal. As this study is concerned with charge density refinements, the remainder of the fitting was performed using on-axis PED simulations because these are a better fit to the experimental data at the charge density-sensitive low φ angles.

It is important to note that fitting on-zone (or nearly on-zone) conventional diffraction data with multislice simulations is ill-advised because in multislice it is assumed that the sample is uniformly thick and flat. Therefore, when the thickness-averaged experimental data is fit to single-thickness multislice simulations, somewhat erroneous results may be observed because the effect of multiple scattering may be quite different in the two systems. Therefore, even though the non-precessed data is visibly

Table 1

Exponential decay parameter and correlation coefficient from measured experimental data and simulations using DT, DS, and SCF potentials at a thickness of 102 nm (728 slices)

	I(001)		I(003)	
	D	R^2	D	R^2
Measured	-0.109	0.99	-0.145	0.99
DT	-0.112	0.99	-0.139	0.96
DS	-0.108	0.99	-0.134	0.94
SCF	-0.118	0.99	-0.134	0.94

Table 2

Exponential decay parameters and correlation coefficients for simulations using the DT potential

Slices	Thickness (nm)	I(001)		I(003)	
		D	R^2	D	R^2
200	28	-0.097	0.908	-0.145	0.954
300	42	-0.124	0.977	-0.1834	0.902
400	56	-0.123	0.962	-0.165	0.966
500	70	-0.133	0.972	-0.1665	0.983
600	84	-0.131	0.954	-0.179	0.992
728	102	-0.112	0.986	-0.139	0.963
800	112	-0.130	0.986	-0.166	0.988
900	126	-0.129	0.982	-0.169	0.995
Avg		-0.122	0.966	-0.164	0.968
STD		0.012	0.026	0.015	0.031

Simulation corresponding to the experimentally measured thickness is in bold.

non-symmetric and matches a 0.8–0.9 mrad tilt offset simulation the best, the confidence in the magnitude of the tilt offset is no better than the confidence in the non-precessed thickness measurement discussed previously (see solid line in Fig. 1(a)), which had uncertainty of several percent. Precession simulations were not used to determine the tilt offset in addition to the thickness, as this would be impractical due to the $1000 \times$ computational time penalty which PED simulations incur.

3.3. Charge density

The global minimum R -factor was computed for all experimental PED semiangles compared to the DT, DS, and SCF potentials in order to determine the observability of charge density effects (Fig. 4). See Table 3 for a complete list of R -factors and relative improvements from using the SCF potential. Of the three potentials used, only SCF incorporates bonding effects and is in principle the most correct. At low precession angles (< 18 mrad) the SCF fit is superior to both the DT and DS cases indicating that the experimental data is sensitive to bonding effects at these precession angles. For the 6.5 and 13 mrad φ , the SCF fit is more than 14% better than the DT neutral atom fit and more than 4% better than the DS neutral atom fit. This

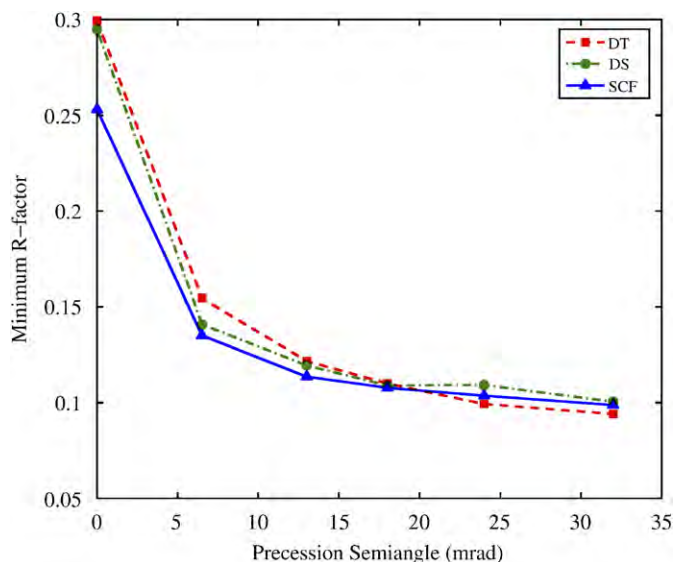


Fig. 4. Plot of minimum R -factor vs. precession semiangle for the DT, DS, and SCF potentials.

Table 3
 R -factors for the DT, DS, and SCF potentials and percent difference between R -factors for these potentials

	DT	DS	SCF	DT–SCF (%)	DS–SCF (%)
0 mrad	0.2994	0.2948	0.2530	18.4	16.5
6.5 mrad	0.1545	0.1409	0.1352	14.3	4.2
13 mrad	0.1218	0.1195	0.1136	7.2	5.2
18 mrad	0.1100	0.1090	0.1078	2.0	1.1
24 mrad	0.0994	0.1092	0.1037	−4.1	5.3
32 mrad	0.0941	0.1006	0.0988	−4.8	1.8

Only the SCF potential incorporates bonding effects.

finding combined with the large improvement in data quality (and lower R -factor) of even low precession angles compared with non-precessed experiments implies that it should indeed be possible to refine the valence charge density against an experimental PED dataset to some degree and that this is best accomplished at low tilt angles.

Although the R -factors are the lowest for all potentials at large precession angles, the convergence of the different potentials to $R \sim 0.1$ above 18 mrad implies that the experimental data is relatively insensitive to bonding effects at these angles. We believe this to be due in part to the fact that neither the SCF nor DS potentials are fully 3-D (since they represent only an averaged string potential as previously discussed) while the DT potential utilizes eight independent slices in the z -direction. The SCF R -factor is consistently superior to DS even at high angles, implying the charge density model is better than the neutral atom approximation (as expected); however, at high angles the 2-D assumption of the DS and SCF potentials begins to break down and the neutral atom DT potential produces the best-fit to the experimental data even though it is a less accurate model. We suspect that if a 3-D model that

incorporated the full charge density of the crystal was used, it would continue to outperform the DT model even at high angles, but that is the subject for another study.

4. Conclusion

We have shown experimentally and confirmed with simulation that the decay of kinematically forbidden intensities is exponential as a function of precession angle. This functional form appears to be independent of the form of the potential used in the simulation as well as the thickness of the specimen. Thus the exponential form is rather robust for the kinematically forbidden reflections studied herein, though it is not implicit that other forms of extinction such as those which are accidentally forbidden due to special sites (i.e. the Si(222) reflection) or those due to special Wyckoff atomic sites should behave similarly. Addressing the effect of PED on these other forms of extinction is the subject of a future study.

When PED is applied to provide intensity data used to solve and refine unknown structures, we recommend that atomic positions be first refined against conventional neutral atoms at large precession angles (> 24 mrad) where the PED data is most kinematical (particularly in the structure-defining $0.25\text{--}1.0 \text{ \AA}^{-1}$ range) [19]. During this phase of refinement, a simple neutral atom DT model for the potential may be used and indeed appears to be the most successful for this system at large ϕ . The valence density may then be refined against low-angle PED data most sensitive to subtle bonding effects using a multipole expansion or some other functional form [1] with atomic core positions fixed at their previously refined values.

Acknowledgments

This work was supported by the Department of Energy under Contract DE-FG02-01ER45945/A006 (JC, LDM, BD) as well as the Fannie and John Hertz Foundation (CSO). The authors would like to acknowledge the support of UOP LLC for use of microscopes and support of precession instrumentation (WS).

References

- [1] P. Coppens, X-ray Charge Densities and Chemical Bonding, Oxford University Press, Oxford, 1997.
- [2] P. Coppens, B. Iversen, *Coord. Chem. Rev.* 249 (2004) 179.
- [3] T.S. Koritsanzky, P. Coppens, *Chem. Rev.* 101 (2001) 1583.
- [4] J. Ciston, L.D. Marks, R. Feidenhans'l, et al., *Phys. Rev. B* 74 (2006) 085401.
- [5] B. Jiang, J.M. Zuo, N. Jiang, et al., *Acta Crystallogr. Sect. A* 59 (2003) 341.
- [6] B. Jiang, J.M. Zuo, Q. Chen, et al., *Acta Crystallogr. Sect. A* 58 (2002) 4.
- [7] J.M. Zuo, J.C.H. Spence, M. O'Keefe, *Phys. Rev. Lett.* 61 (1988) 353.
- [8] J.M. Zuo, M. Kim, M.O. O'Keefe, et al., *Nature* 401 (1999) 49.
- [9] K. Tsuda, Y. Ogata, K. Takagi, et al., *Acta Crystallogr. Sect. A* 58 (2002) 514.

- [10] R. Holmestad, C.R. Birkeland, K. Marthinsen, et al., *Microsc. Res. Tech.* 46 (1999) 130.
- [11] R. Holmestad, C.R. Birkeland, *Philos. Mag. A* 77 (1998) 1231.
- [12] W. Nuchter, A.L. Weickenmeier, J. Mayer, *Phys. Status Solidi A* 166 (1998) 367.
- [13] K. Gjønnes, N. Boe, *Micron* 25 (1994) 29.
- [14] M. Saunders, P.A. Midgley, R. Vincent, in: *Electron Microscopy and Analysis*, vol. 147, 1995, p. 125.
- [15] P.A. Midgley, M. Saunders, *Contemp. Phys.* 37 (1996) 441.
- [16] M. Saunders, A.G. Fox, P.A. Midgley, *Acta Crystallogr. Sect. A* 55 (1999) 471.
- [17] R. Vincent, P.A. Midgley, *Ultramicroscopy* 53 (1994) 271.
- [18] J. Gjønnes, V. Hansen, B.S. Berg, et al., *Acta Crystallogr. Sect. A* 54 (1998) 306.
- [19] C.S. Own, L.D. Marks, W. Sinkler, *Acta Crystallogr. Sect. A* 62 (2006) 434.
- [20] A. Avilov, K. Kuligin, S. Nicolopoulos, et al., *Ultramicroscopy* 107 (2007) 431.
- [21] J.P. Morniroli, A. Redjaimia, S. Nicolopoulos, *Ultramicroscopy* 107 (2007) 514.
- [22] M. Gemmi, X.D. Zou, S. Hovmoller, et al., *Acta Crystallogr. Sect. A* 59 (2003) 117.
- [23] C.S. Own, W. Sinkler, L.D. Marks, *Ultramicroscopy* 106 (2006) 114.
- [24] T.E. Weirich, J. Portillo, G. Cox, et al., *Ultramicroscopy* 106 (2006) 164.
- [25] K. Boulahya, L. Ruiz-Gonzalez, M. Parras, et al., *Ultramicroscopy* 107 (2007) 445.
- [26] A.P. Dudka, A.S. Avilov, S. Nicolopoulos, *Ultramicroscopy* 107 (2007) 474.
- [27] W. Taylor, *Z. Kristallogr.* 71 (1929) 205.
- [28] J.K. Winter, S. Ghose, *Am. Mineral.* 64 (1979) 573.
- [29] B. Deng, L.D. Marks, *Acta Crystallogr. Sect. A* 62 (2006) 208.
- [30] C.S. Own, L.D. Marks, W. Sinkler, *Rev. Sci. Instrum.* 76 (2005).
- [31] R. Kilaas, L.D. Marks, C.S. Own, *Ultramicroscopy* 102 (2005) 233.
- [32] R. Kilaas, C.S. Own, B. Deng, et al., EDM: Electron Direct Methods: Documentation-2.0.1, <<http://www.numis.northwestern.edu/edm/documentation/edm.htm>>, (2006).
- [33] P. Xu, G. Jayaram, L.D. Marks, *Ultramicroscopy* 53 (1994) 15.
- [34] P.A. Doyle, P.S. Turner, *Acta Crystallogr. Sect. A* 24 (1968) 390.
- [35] J.M. Cowley, A.F. Moodie, *Acta Crystallogr.* 10 (1957) 609.
- [36] P. Goodman, A.F. Moodie, *Acta Crystallogr. Sect. A* 30 (1974) 280.
- [37] P. Blaha, K. Schwarz, P. Sorantin, et al., *Comput. Phys. Commun.* 59 (1990) 399.
- [38] P. Blaha, K. Schwarz, G.K.H. Madsen, et al., WIEN2k, An Augmented Plane Wave+Local Orbitals Program for Calculating Crystal Properties, Vienna University of Technology, Vienna, 2001.
- [39] J.P. Perdew, K. Burke, Y. Wang, *Phys. Rev. B* 54 (1996) 16533.
- [40] I.P. Grant, B.J. McKenzie, P.H. Norrington, et al., *Comput. Phys. Commun.* 21 (1980) 207.
- [41] T. Hahn (Ed.), *International Tables for Crystallography*, vol. A, Kluwer, Dordrecht, 1989.
- [42] J. Gjønnes, A.F. Moodie, *Acta Crystallogr.* 19 (1965) 65.